TECHNISCHE MECHANIK, 30, 1-3, (2010), 29- 44
submitted: November 13, 2009

Modelling of precipitation during friction stir welding of an Al-Mg-Si alloy

D. Carron, P. Bastid, Y. Yin, R.G. Faulkner

In this study, microstructural evolution in AA 6082-T651 friction stir welds is simulated using a metallurgical model coupling a Monte Carlo random sampling technique and classical nucleation and growth theory. The calculated volume fraction and size distribution of precipitates are used to predict hardness. Some of the model parameters are calibrated from microstructure and hardness data available in the open literature. Temperature and hardness data in the region of the weld are obtained from FSW experiments. The temperature in the weld is predicted by finite element analysis, with a simplified thermo-mechanical approach, after calibration of heat transfer parameters in order to match the temperature measurements. The calculated thermal cycles are then applied to the metallurgical model. The subsequently predicted hardness profiles across the weld are then compared with experimental data.

1 Introduction

Friction stir welding (FSW) is a relatively new solid-state joining method in which a rotating tool is used to heat and mix material across the joint (Thomas, 1991; Mishra and Ma, 2005). This process generates large local deformations and heat cycles, which consequently modify the microstructure and mechanical properties of several zones in the joint. The central region, called the weld nugget (WN), is highly deformed and fully recrystallised. Next to the WN the thermomechanically affected zone (TMAZ) also experiences high deformation, but insufficient to lead to recrystallisation. Further away from the WN the heat affected zone (HAZ) undergoes little or no deformation, but thermal cycles still affect the microstructure. In Al-Mg-Si age hardened alloys the microstructure evolution generally consists of a combination of dissolution, coarsening and reprecipitation of strengthening precipitates (Mishra and Ma, 2005).

The AA 6082 alloy considered in this work is a low copper and low excess silicon content Al-Mg-Si alloy. Its strong age-hardening response is the result of nucleation and growth in the aluminium matrix of different types of metastable precursors of the equilibrium β-Mg_2Si phase. The complex precipitation sequence contains many steps and may be simplified as follows (Ravi and Wolverton, 2004; Chakrabarti and Laughlin, 2004): SSSS → Atomic clusters → GP-zones → β″ → β′ → β. Precipitation from the super-saturated solid solution (SSSS) starts with solute clustering, which is then followed by the formation of Guinier-Preston (GP) zones, fully coherent with the matrix. Formation of GP zones is favoured by low temperature artificial ageing or natural ageing (NA) at room temperature. They provide moderate hardening. The presence of the needle-like coherent β″-Mg_5Si_6 precipitates, which evolve from the GP zones and are generally found in alloys aged to peak hardness (T6 condition), is associated with the optimal mechanical properties of these alloys. The rod-shaped β′-$Mg_{1.7}Si$ incoherent (or semi-coherent) precipitates, as well as the equilibrium β-Mg_2Si phase platelets, are characteristic of overaged conditions which exhibit reduced mechanical properties. Actually the precipitation sequence is considerably more complex than the generic sequence given above and some controversy still remains. In FSW AA6082-T6 welded plates, β″ was reported to be homogeneously dispersed in the unaffected base material but to have been dissolved both in the WN, the TMAZ and in the main part of the HAZ (Svennson et al., 2000; M.J. Peel et al., 2006). During cooling of the weld, precipitation of particles which are less effective at hardening, such as β′, takes place rapidly in the HAZ region of minimum hardness. In the nugget zone with higher peak temperatures all β″ precipitates dissolve but β′ precipitation does not take place because of high cooling rates. In the regions where dissolution occurs, NA might cause some precipitation of GP zones.

The optimization of FSW requires the development of predictive models to understand and quantify the effects of the numerous process and materials parameters. Semi-empirical approaches have been developed by Russell and Shercliff (1999) and Robson et al. (2004) which successfully predicted hardness profiles after FSW but without providing a detailed description of the precipitation evolution. Precipitation evolution during FSW of aluminium

alloys has been recently successfully modelled (Simar et al, 2007; Kamp et al., 2006; Kamp et al., 2007; Gallais et al., 2008) using mesoscale "size class" approaches based on classic kinetic theory and the Kampmann and Wagner numerical (KWN) framework (Kampmann and Wagner, 1991). The aim of this work is to predict the state of precipitation and the subsequent hardness profiles across FSW welds. The precipitation model used here couples a Monte Carlo random sampling technique and classical nucleation and growth theory and has been recently developed by Yin and Faulkner (2003) for predicting precipitation kinetics in ferritic steels. Combined with continuum creep damage mechanics, the precipitation model has been used to predict the creep rate of power plant steels at any specified time and temperature (Yin and Faulkner, 2005; Yin and Faulkner, 2006). Irradiation induced precipitation has also been modelled (Yin and Faulkner, 2009). This model allows the prediction of precipitate size, volume fraction, and inter-precipitate spacing as a function of both time and temperature.

The present paper is structured as follows. Materials and experimental methods are first presented. The thermal, precipitation and hardening models are then detailed. The model parameters are identified using microstructure and hardness data available in the open literature. Finally the results of FSW modelling are discussed through the comparison of predicted and experimental hardness profiles across the weld.

2 Materials and experimental methods

The composition of the AA 6082 alloy (EN AW-6082 / AlSi1MgMn) under study is given in Table 1. Prior to simulating the precipitation during FSW, some of the precipitation and strength model parameters were calibrated from microstructure and hardness data available in the open literature for the ageing of an experimental Al-Mg-Si alloy (Myhr et al., 2001) which has a composition that slightly differs from that of AA 6082 (see Table 1). These data were used by Myhr et al. (2001) to simulate the precipitation with a "size class model" that is a finite difference formulation of the classical KWN precipitation model. The heat treatments applied to the alloys are given in Table 2. The AA 6082 alloy is welded from the T651 condition. This designation applies to products in T6 temper which, after quenching, undergo controlled stretching to relieve internal stresses. Since work hardening is not taken into account in the strength modelling, T6 or T651 conditions are considered here as equivalent for the purpose of simulation.

Alloy	*Si*	*Mg*	*Cu*	*Mn*	*Fe*	*Cr*	*Ti*	*Zn*	*Ga*	*Al*
Al-Mg-Si	0.82	0.55	0.016	0.5	0.2	-	-	-	-	balance
6082	1.07	0.71	-	0.59	0.24	-	0.009	0.02	0.009	balance

Table 1. Chemical composition of aluminium alloys (in wt%). Data for the experimental Al-Mg-Si alloy are taken from Myhr et al. (2001)

Alloy	*Thickness*	*Solution Heat treatment*	*Quench medium*	*Artificial ageing*
Al-Mg-Si	3 mm	530°C - 30 min	water	185°C (various times)
6082	6 mm	530°C - 50 min	water	175°C (8h for T6 temper)

Table 2. Conditions for solution heat treatment, quenching and hardening. Data for the experimental Al-Mg-Si alloy and 6082 alloy are respectively taken from Myhr et al. (2001) and Alcan (2004)

Two AA 6082 plates were joined using a Transformation Technologies Inc (TTI) FSW machine at TWI Sheffield. The plates are 1000 mm in length, 125 mm in width and 6 mm in thickness. The tool rotational and welding speeds were 800 rpm and 800 mm/min respectively. Plates lay on a steel table. Welding parameters (speeds, forces and torque) are recorded during the FSW process. Temperatures profiles are measured during welding. The plates were instrumented with thermocouples at the mid-thickness of the plates at 14, 17 and 22 mm from the weld centre line in order to measure the gradient in the direction transverse to the weld. Some thermocouples were also introduced in the through-thickness direction at 3 mm and 5 mm from the upper face. Cross section macrographs did not show any defects. Plates were naturally aged after welding. Mid-thickness hardness profiles (HV1 measurements) were obtained using a Shimadzu Micro Hardness Tester on the cross

section of the weld in the steady state area. Hardness measurements were performed three weeks after welding so any postweld NA would have been substantially complete.

3 Thermal modelling

The temperature field in the welded AA 6082 plates was predicted using the finite element (FE) analysis software Abaqus™. The main objective of the model was the prediction of the steady-state temperature history at points where the temperature could not be measured by thermocouples, especially in the section of the plates below the tool shoulder. Only solid heat transfer was considered in the chosen thermo-mechanical approach. The material flow was not modelled. However, the heat generated by the visco-plastic deformation was included. This represents a simplification compared with more fundamental approaches that use computational fluid dynamics to model the underlying physical processes (Smith, 2004).

Symmetry about the vertical plane passing through the weld centre line has been assumed. Because of this assumption, the rotation of the tool, and the asymmetry of the heat source at the advancing and receding sides of the weld were not taken into account. The plate and table were meshed with Abaqus™ DC3D8-type heat transfer elements with linear interpolation. The element size was 1mm in the direction transverse to the weld where predicted temperature cycles were required. The mesh is shown in Figure 1.

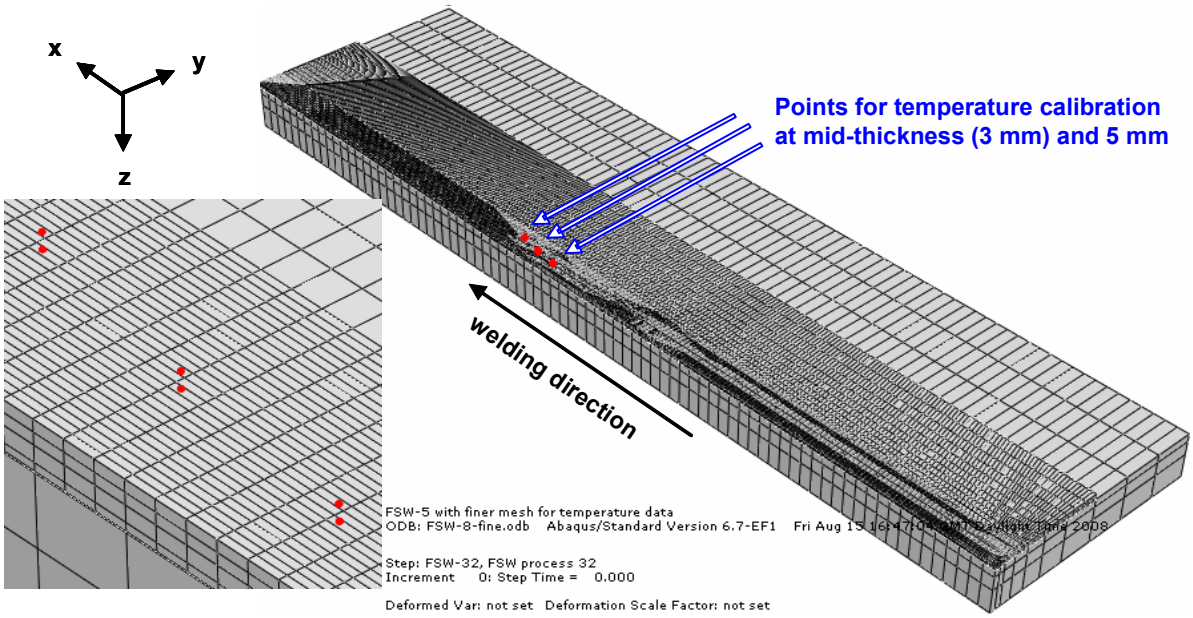

Figure 1. Mesh of the plate and table showing the position of the nodes for calibration of heat transfer coefficients by comparison of predicted and measured temperature values

A simplifying assumption was made that the material sticks to the tool and that heat is generated by plastic deformation, allowing use of a volumetric heat source. Figure 2 shows the region where the heat is generated.

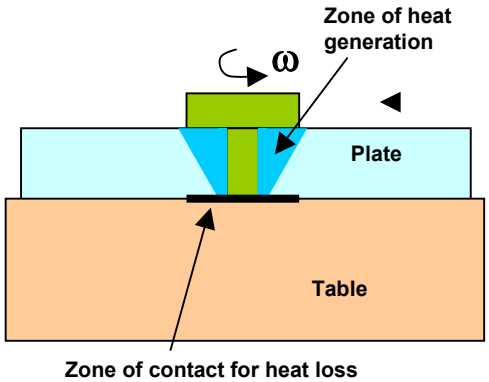

Figure 2. Sketch showing the heat source region and contact interface

The power input per unit volume in the zone of heat generation is given by

$$H_v = A\,\omega\, r\,\tau \quad with \quad \tau = \frac{1}{\sqrt{3}}\sigma \tag{1}$$

where A is a calibration parameter, ω is the tool rotation speed, r is the distance from the tool axis, τ is the shear stress and σ is the Von Mises stress. σ was assumed to vary with temperature only and its value was determined from tensile strain-stress curves (not presented here). This description of the heat generation is adequate for material points close to the pin and shoulder of the tool. However, when the distance from the tool increases, the effect of the strain rate decreasing is not captured. The model therefore overestimates the heat produced by the deformation and the calibration parameter A is required to reduce the heat input.

The boundary conditions used for the model are as follows: natural convection between aluminium and air on the faces of the plate that are not in contact with the table; heat conduction between aluminium and steel at the bottom surface. The thermal properties of the plate are those for AA 6005 alloy given in Simar et al. (2006). Convection was modelled using a heat transfer coefficient equal to 12 $W.m^{2}.K^{-1}$ and an ambient temperature equal to 20°C. Defining the contact conditions between the table and plate is extremely complex. The following simplification was therefore judged to be acceptable. Three different regions are defined at the interface: below the tool where the contact is almost perfect because of the pressure; below the weld where the contact is poorer; and on the rest of surface of the table where heat transfer does not take place. This contact condition is imposed in the FE code by artificially introducing a material layer of 0.2 mm thickness with variable contact conductivity (Simar et al., 2006). The surface heat flux was given by:

$$Q_s = K\,(T_{table} - T_{plate}) \tag{2}$$

where K is the contact conductivity defined for each region.

The calibration of the model has been achieved by fitting modelled thermal curves to experimental results to determine A and K parameters. Using the values of A = 0.003 and K = 500 $W.m^{-2}.K^{-1}$ (same value for the surface below the tool and the surface below the weld) generated the temperature prediction shown in Figure 3.

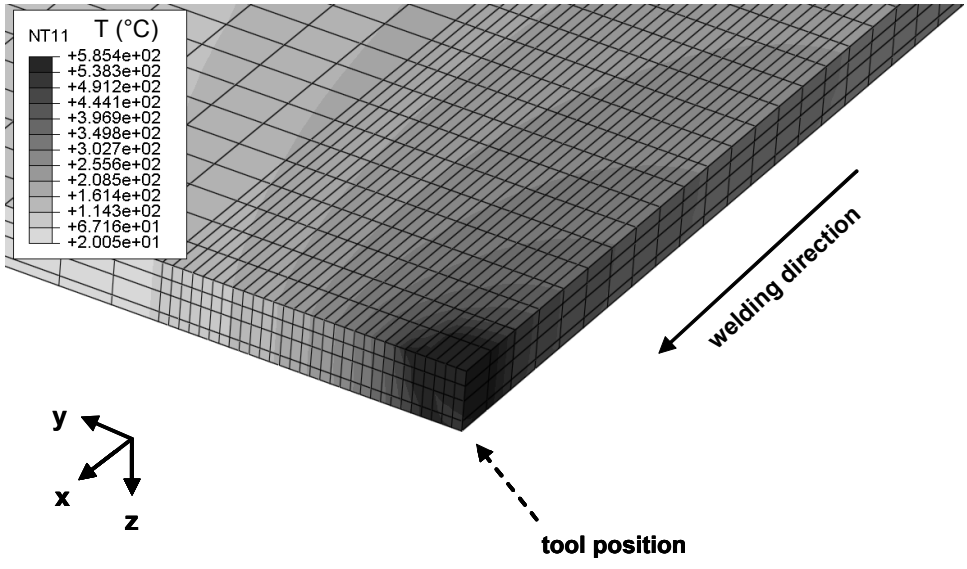

Figure 3. Predicted temperature distribution in the FSW welded plate. The tool is located at x = 600mm

Figure 4 shows the comparison between predicted and experimental measurements from the thermocouples at mid-thickness.

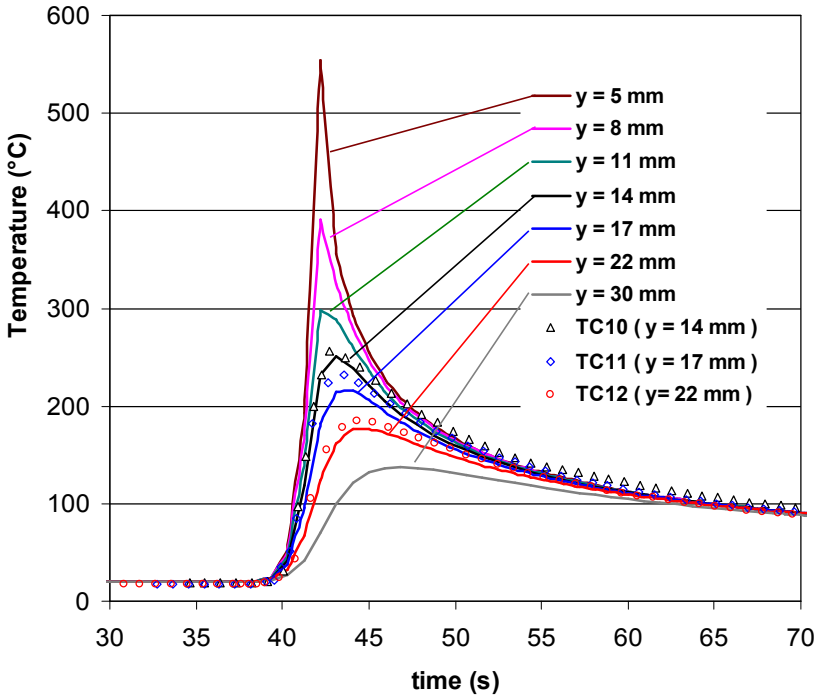

Figure 4. Comparison between predicted (x = 600 mm) and measured temperature values at mid-thickness after calibration of the heat transfer parameters. Predicted and experimental cycles are represented by lines and symbols respectively

The agreement between the model and the experiments is satisfactory considering the steep thermal gradients in the transverse direction and possible inaccuracy in the locations of the thermocouples. Good agreement was also found while comparing predicted and experimental cycles at 5 mm from the upper face (not shown here). This agreement gives confidence for extrapolating the calculated thermal history to areas closer to the central position of the tool where material flow takes place, which is not taken into account by the model.

4 Precipitation model

The model has been described in full detail elsewhere (Yin and Faulkner, 2003). However a brief description is given here below, together with the modifications introduced for modelling precipitation in Al-Mg-Si alloys.

4.1 Simulation cell

The simulation is carried out in a representative body of the material termed the simulation cell, which can include both matrix and grain boundaries. The model can consider the nucleation, growth and coarsening of inter- and intra-granular precipitates separately. Quench induced solute segregation to the grain boundaries is taken into account according to the non-equilibrium segregation model developed by Faulkner (1987). For 6XXX Al-Mg-Si alloys, considering the difficulty of taking into account the complex precipitation sequence described in the introduction, only Mg_2Si spherical intra-granular precipitation is considered. Thus the segregation effect is not considered in the simulation process, initial solute concentration after the solution heat treatment is taken as homogeneous in the alloy, and inter-granular nucleation is inhibited.

4.2 Nucleation

The heat treatment (ageing, welding) is then divided into many small time intervals. Nucleation of precipitates is considered. The number of nuclei generated in each time step is calculated according to the classical nucleation theory which gives the nucleation rate as

$$I = N_0 Z \beta^* \exp\left(-\frac{\Delta G^*}{kT}\right)\exp\left(-\frac{\tau}{t}\right) \tag{3}$$

where N_0 is the number of nucleation sites per unit volume, Z is the Zeldovich factor, β^* is the frequency factor i.e. the rate at which solute atoms are added to the nucleus, ΔG^* is the activation energy required to form the critical nucleus, k is the Boltzmann constant, T is the absolute temperature, t is the time and τ is the incubation time for nucleation. The expressions used for Z, β^* and τ are those given in Yin and Faulkner (2003).

Due to the presence of dispersoids, dislocations, clusters, GP zones and others material inhomogeneities, which may act as nucleation sites for the precipitates, intra-granular nucleation is essentially heterogeneous in 6xxx aluminium alloys. This is modelled by adapting homogeneous nucleation theory to account for the limited number of nucleation sites and the reduced energy barrier to nucleation as follows. The number of nucleation sites per unit volume N_0 is treated as an adjustable parameter (Samaras, 2006). The reduction in the energy barrier required to form the critical nucleus is taken into account by the introduction of an adjustable parameter in the expression of ΔG^*. This approach is similar to those used by Deschamps and Brechet (1999) and Myhr et al. (2000) to describe heterogeneous nucleation in Al-Zn-Mg and Al-Mg-Si alloys respectively. Ignoring strain energy, ΔG^* is then determined for spherical precipitates as follows

$$\Delta G^* = k_{\Delta G^*} \frac{16\pi\gamma^3}{3\Delta G_V^2} \tag{4}$$

where $k_{\Delta G^*}$ is an adjustable parameter, γ is the interfacial energy of the particle and ΔG_V is the chemical free energy change driving nucleation. ΔG_V is calculated according to the assumptions of the growth model (see below). The critical radius r^* for nucleus formation depends on ΔG_V as follows

$$r^* = \frac{-2\gamma}{\Delta G_V} \tag{5}$$

The model constructs an array of potential nuclei using a Monte Carlo random sampling algorithm so that a distribution of spatially defined particles is formed and monitored throughout the heat treatment of the material. Nuclei of critical size are generated and located randomly within the simulation cell. At each time step, the number of nuclei generated, ΔN, is limited by

$$\Delta N = I\,\Delta t \tag{6}$$

where I is the nucleation rate determined using equation (3). Because the decreasing solute concentration lowers the activation energy for nucleation, ΔG^*, and reduces the supply term, β^*, the nucleation rate approaches zero as the solute saturation level approaches equilibrium.

4.3 Growth and coarsening

All the precipitates formed before or during the considered time step are individually allowed to either grow or dissolve. The growth or dissolution of a precipitate of composition Mg_2Si embedded in the aluminium matrix is determined by a diffusion controlled growth rate given by (Perez et al., 2008).

$$\frac{dr}{dt} = \frac{D_{Mg}}{r}\frac{\overline{X}_{Mg} - X^i_{Mg}(r)}{\frac{\upsilon^\alpha_{at}}{\upsilon^\beta_{at}}X^\beta_{Mg} - X^i_{Mg}(r)} = \frac{D_{Si}}{r}\frac{\overline{X}_{Si} - X^i_{Si}(r)}{\frac{\upsilon^\alpha_{at}}{\upsilon^\beta_{at}}X^\beta_{Si} - X^i_{Si}(r)} \tag{7}$$

where D_E is the diffusivity of the element E *(E = Mg, Si)* in the matrix, r is the radius of the precipitate, $\overline{X}_E$ is the mean atomic fraction of E in the matrix, X^β_E is the equilibrium atomic fraction of E in the precipitate, $X^i_E(r)$ is the equilibrium atomic fraction of E at the precipitate/matrix interface, and υ^α_{at} and υ^β_{at} are the matrix and precipitate mean atomic volumes (mean volume per atom) respectively.

Since the composition of the precipitate in matrix is assumed to be pure Mg_2Si, the ratio of matrix to precipitate atomic volumes is given by

$$\frac{\upsilon_{at}^{\alpha}}{\upsilon_{at}^{\beta}} = \frac{3V_{\alpha}}{V_{\beta}} \tag{8}$$

where V_β is the molar volume of the precipitating phase (volume of one mole of Mg_2Si) and V_α is the molar volume of the aluminium matrix.

The diffusivity is written as

$$D_E = D_E^0 \exp\left(-\frac{Q_E}{RT}\right) \tag{9}$$

where D_E^0 and Q_E are the volume diffusion pre-exponential term and activation energy respectively, and R is the universal gas constant. The diffusivity of magnesium and silicon atoms in aluminium are considered to be essentially the same in Al-Mg-Si alloy (Myhr et al, 2001).

$X_{Mg}^i(r)$ and $X_{Si}^i(r)$ depend on the particle radius due to the influence of interfaces on equilibrium (Gibbs-Thomson effect). This is taken into account through (Perez, 2005).

$$X_{Mg}^i(r)^2\ X_{Si}^i(r) = X_{Mg}^i(\infty)^2\, X_{Si}^i(\infty)\exp\left(\frac{2\gamma V_\beta}{rRT}\right) \tag{10}$$

where $X_{Mg}^i(\infty)$ and $X_{Si}^i(\infty)$ are the equilibrium atomic fraction of magnesium and silicon, respectively, in the matrix for a planar interface.

From the solubility product we have

$$X_{Mg}^i(\infty)^2\ X_{Si}^i(\infty) = \exp\left(-\frac{\Delta H^0}{RT} + \frac{\Delta S^0}{R}\right) \tag{11}$$

where $\Delta S°$ and $\Delta H°$ are the entropy and enthalpy, respectively, associated with the precipitation/dissolution of the precipitating phase.

The volume fraction of precipitates V_f being known from the previous iteration, and assuming silicon is present in overstoichiometric amount, the mean atomic fraction of magnesium in the matrix is determined from

$$\overline{X}_{Mg} = X_{Mg}^0\left(1 - \frac{V_f}{V_f^{\max}}\right) \tag{12}$$

where X_{Mg}^0 is the nominal magnesium atomic fraction and $V_f^{\max}$ is the maximum volume fraction given by

$$V_f^{\max} = \frac{X_{Mg}^0 V_\beta}{2V_\alpha} \tag{13}$$

Considering the stoichiometry of the reaction of precipitation/dissolution and the influence of Fe and Mn on the silicon solid solubility due to the formation of intermetallic phases, the mean atomic fraction of silicon in the matrix is obtained by

$$\overline{X}_{Si} = X_{Si}^{eff} - \frac{1}{2}\left(X_{Mg}^{0} - \overline{X}_{Mg}\right) \tag{14}$$

where X_{Si}^{eff} is the effective silicon atomic fraction in the alloy given by (Myhr et al, 2001)

$$X_{Si}^{eff} = X_{Si}^{0} - \frac{2}{3}\left(X_{Fe}^{0} + X_{Mn}^{0}\right) \tag{15}$$

where X_{Si}^{0}, X_{Fe}^{0} and X_{Mn}^{0} refer to the nominal Si, Fe and Mn atomic fractions respectively.

Once $\overline{X}_{Mg}$ and $\overline{X}_{Si}$ are calculated, equations (7) and (10) are solved to determine the growth rate of a given particle. For each particle the growth rate can be positive or negative leading to growth or dissolution respectively. The coarsening phenomenon - i.e. growth of larger particles at the cost of dissolution of small particles - is thus naturally described by the model. The value of the critical radius *r** - i.e. the radius of a particle that will neither grow nor dissolve - can also be easily expressed from equation (7) and (10). Using equation (5) the chemical free energy change driving nucleation is then given for the next time step by

$$\begin{aligned}\Delta G_v &= -\frac{RT}{V_\beta}\left(2\ln\left(\frac{\overline{X}_{Mg}}{X_{Mg}^{i}(\infty)}\right) + \ln\left(\frac{\overline{X}_{Si}}{X_{Si}^{i}(\infty)}\right)\right) \\ &= -\frac{RT}{V_\beta}\left(2\ln\left(\overline{X}_{Mg}\right) + y\,\ln\left(\overline{X}_{Si}\right) - \left(-\frac{\Delta H^0}{RT} + \frac{\Delta S^0}{R}\right)\right)\end{aligned} \tag{16}$$

The nucleation/growth (or dissolution) process at each time step is repeated for all time intervals until the required time duration of heat treatment is reached and results containing average particle size, particle size distributions, volume fraction and other useful data are obtained as a function of time.

5 Strength model

Precipitation modelling results are applied to a strength model in order to calculate yield strength and hardness values. Five strengthening mechanisms contribute to the overall alloy yield strength: lattice resistance σ_i, grain boundary hardening σ_{gb}, work hardening σ_{wh}, solid solution hardening σ_{ss} and precipitation hardening σ_p. The overall yield strength calculation is generally achieved by adding the various contributions.

$$\sigma_y = \sigma_i + \sigma_{gb} + \sigma_{wh} + \sigma_{ss} + \sigma_p \tag{17}$$

For age hardening aluminium alloys without deformation after the solution heat treatment, the grain size and the dislocation contribution to the flow stress are assumed to be negligible. For friction stir welded Al-Mg-Si alloys the same hypothesis was made according to Simar et al. (2007). Thus the equation above is reduced to

$$\sigma_y = \sigma_i + \sigma_{ss} + \sigma_p \tag{18}$$

The σ_i value is taken to be equal to the intrinsic yield strength of pure aluminium. The solid solution strengthening σ_{ss} depends of the concentrations of Mg, Si and Cu elements and can be expressed as (Myhr et al., 2001)

$$\sigma_{ss} = \sum_j k_j \left(C_j^{wt}\right)^{2/3} \tag{19}$$

where C_j^{wt} is the concentration (in wt%) of a specific alloying element in solid solution and k_j the corresponding scaling factor. In our case, for the Mg and Si elements, these concentrations are obtained from the calculated atomic concentrations $\overline{X}_{Mg}$ and $\overline{X}_{Si}$ issued from the microstructure model. The C_{Cu}^{wt} concentration has a constant value coming from the alloy composition.

The precipitation hardening is due to shearing and bypassing of precipitates by dislocations. It is calculated using results for the mean radius, the precipitate size distribution and the volume fraction of precipitates from the microstructure model according to Deschamps and Brechet (1999). σ_p depends on the mean obstacle strength $\overline{F}$ according to

$$\sigma_p = \frac{M\overline{F}}{bl} \tag{20}$$

where M is the Taylor factor, b is the Burgers vector and l is the mean particle spacing along the dislocation line.

Using the Friedel formalism (Friedel, 1964) to estimate l transforms this equation into

$$\sigma_p = \frac{M}{b\bar{r}}\left(2\beta G b^2\right)^{-1/2}\sqrt{\frac{3V_f}{2\pi}}\overline{F}^{3/2} \tag{21}$$

where G is the shear modulus of the aluminium matrix, β is a constant close to 0.5, and $\bar{r}$ is the predicted mean particle radius.

The mean obstacle strength is expressed as

$$\overline{F} = \frac{\sum_{i=1}^{N_p} F_i}{N_p} \tag{22}$$

where F_i is the obstacle strength for a specific particle and N_p is the total number of precipitates in the simulation cell.

According to its size, a precipitate of radius r_i is considered to be sheared or bypassed by the dislocations. As long as r_i is smaller than the critical radius for shearing r_c (which corresponds almost to the radius at the peak hardness), F_i is proportional to the particle radius.

$$F_i = 2\beta G b^2\left(\frac{r_i}{r_c}\right) \tag{23}$$

Above this critical radius, the precipitate is bypassed and F_i is constant and independent of r_i.

$$F_i = 2\beta G b^2 \tag{24}$$

Different sets of values for M and β can be found in the literature. However, according to Samaras (2006), the various parameters in equation (21) can be reduced to one which can be calibrated by experiment.

$$k_p = 2\beta b G M\sqrt{\frac{3}{2\pi}} \tag{25}$$

The precipitation hardening contribution is finally given by

$$\sigma_p = k_p\frac{\sqrt{V_f}}{\bar{r}N_p}\left(\sum_{i=1}^{N_p} f\left(r_i\right)\right)^{3/2} \quad with \begin{cases} f\left(r_i\right) = \dfrac{r_i}{r_c} & if\ r_i < r_c \\ f\left(r_i\right) = 1 & if\ r_i > r_c \end{cases} \tag{26}$$

In order to predict the increase in yield strength in the friction stir welded region subjected to NA a model coming from Simar et al. (2007) which follows the formalism of Esmaeili et al. (2003) has been used. Because a

low magnesium concentration does not favour the precipitation of GP zones, it was considered that NA only occurs when the magnesium concentration exceeds a certain amount $\overline{X}_{Mg\,\lim}$. In these zones the overall yield strength is given by

$$\sigma_{na} = \sigma_y + k_{na}\sqrt{\frac{\overline{X}_{Mg} - \overline{X}_{Mg\,\lim}}{X^0_{Mg} - \overline{X}_{Mg\,\lim}}} - \sigma_{SS}(C^{wt}_j) + \sigma_{SS}(C^{wt}_{j\,\lim}) \tag{27}$$

where k_{na} is a constant and σ_y is the yield strength defined in equation (18). $\sigma_{SS}(C^{wt}_{j\,\lim})$ is the solid solution strengthening contribution calculated from equation (19) with the remaining alloying element concentrations of the NA regions. $\overline{X}_{Mg\,\lim}$ and k_{na} are determined in order to obtain the minimum hardness experimental value in the FSW plates and an ultimate hardness value of 80 HV (hardness of a solution heat treated 6082 alloy after 5-7 days of natural ageing) in the limiting case where $\overline{X}_{Mg} = X^0_{Mg}$.

Conversion from yield strength (in MPa) to hardness HV (in Vickers) can be done for Al-Mg-Si alloys with (Myhr et al., 2001)

$$HV = 0.33\sigma_y + 16 = 0.33\left(\sigma_0 + \sigma_{ss} + \sigma_p\right) + 16 \tag{28}$$

6 Input data

The input data for the microstructure and strength models are summarised in Table 3 and Table 4.

The microstructural parameter calibration ($D°_{Mg}$, N_0, γ, $k_{\Delta G*}$) was essentially achieved using the experimental Al-Mg-Si alloy ageing data given in Myhr et al. (2001). $k_{\Delta G*}$ was considered as a parameter specific to the alloy (experimental Al-Mg-Si or AA 6082). k_p was optimised to obtain the correct peak hardness value. $\overline{X}_{Mg\,\lim}$ and k_{na} were optimised with regards to the experimental FSW hardness profiles (see above).

Symbol	*Parameter*	*Value*	*Unit*	*Origin*
X^0_{Mg}	Nominal magnesium concentration	specific to the alloy	at. fraction	Table 1
X^{eff}_{Si}	Effective silicon concentration	specific to the alloy	at. fraction	Table 1 and equation (12)
a	Matrix lattice parameter	0.404	nm	Hatch (1984)
V_α	Molar volume, matrix	$1\text{x}10^{-5}$	$m^3.mol^{-1}$	Hatch (1984)
V_β	Molar volume, Mg_2Si	$3.95\text{x}10^{-5}$	$m^3.mol^{-1}$	Grong (1997)
D^0_{Mg}	Volume diffusion pre-exponential term	$6.0\text{x}10^{-4}$	$m^2.s^{-1}$	optimised
Q_{Mg}	Volume diffusion activation energy	130000	$J.mol^{-1}$	Grong (1997)
$\Delta H°$	Enthalpy of Mg_2Si precipitation/dissolution	95900	$J.mol^{-1}$	Grong (1997)
$\Delta S°$	Entropy of Mg_2Si precipitation/dissolution	112	$J.mol^{-1}.K^{-1}$	Grong (1997)
γ	Interfacial energy	0.8	$J.m^{-2}$	optimised
$k_{\Delta G^*}$	Adjustable parameter in the activation energy for nucleation	0.0042 Al-Mg-Si 0.0054 6082	-	optimised
N_0	Number of nucleation sites per unit volume	$9.0\text{x}10^{22}$	m^{-3}	optimised

Table 3. Summary of input data used in the microstructure model. $\Delta H°$ and $\Delta S°$ values are defined for concentrations in at.% in the solubility product

Symbol	*Parameter*	*Value*	*Unit*	*Origin*
σ_i	Intrinsic yield strength of pure aluminium	10	MPa	Myhr (2001)
C_{Cu}^{wt}	Nominal Mg concentration	specific to the alloy	wt%	Table 1
$\overline{X}_{Mg\,\lim}$	Limiting Mg concentration for NA	0.0022	at. fraction	optimised
r_c	Critical radius for shearing	$5x10^{-9}$	m	Myhr et al. (2001)
k_p	Precipitation hardening strength calculation constant	$1.00x10^{-5}$	$MPa.m^{-1}$	optimised
k_{Si}	Solution hardening strength calculation constant for Si	66.3	$MPa.wt\%^{-2/3}$	Myhr et al. (2001)
k_{Mg}	Solution hardening strength calculation constant for Mg	29.0	$MPa.wt\%^{-2/3}$	Myhr et al. (2001)
k_{Cu}	Solution hardening strength calculation constant for Cu	46.4	$MPa.wt\%^{-2/3}$	Myhr et al. (2001)
k_{na}	Natural hardening strength calculation constant	130.1	MPa	optimised

Table 4. Summary of input data used in the strength model

7 Results and discussion

7.1 Ageing of Al-Mg-Si experimental alloy

Figure 5 shows how the particle number density and the mean particle radius vary with time during the ageing at 185°C of the experimental Al-Mg-Si alloy. The particle number density reaches a peak after 1h of ageing before coarsening begins. The mean particle radius continuously increases during ageing. A good agreement is obtained between the experimental and simulated particle number density and mean particle radius except for the overageing response which is stronger than predicted by the model. The maximum particle number density after 1h of ageing seems slightly underestimated.

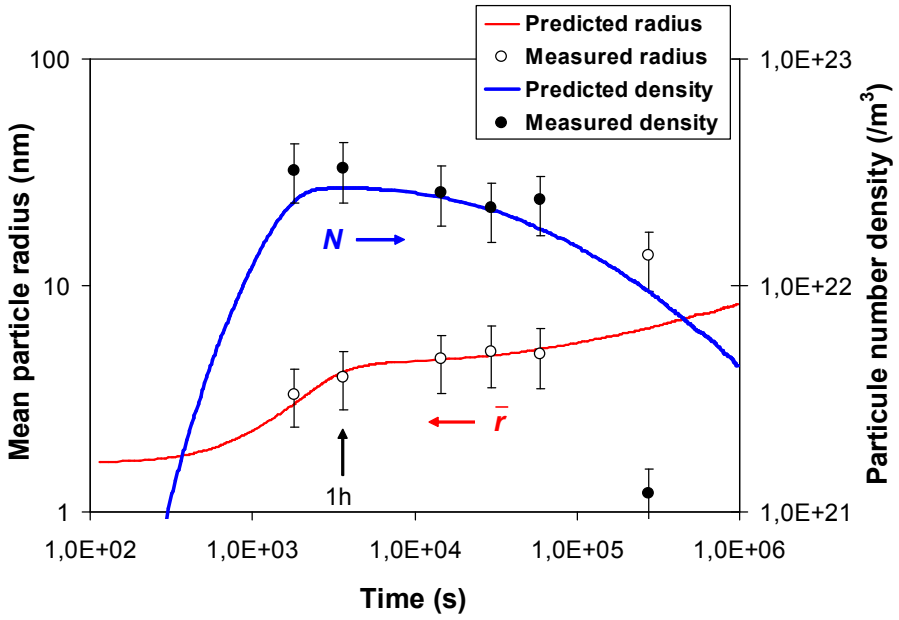

Figure 5. Predicted precipitation kinetics in the experimental Al-Mg-Si alloy during ageing at 185°C. Experimental data from Myhr et al. (2001)

The parameter calibration achieved in this work has led to optimised values that may differ from published ones. The $D°_{Mg}$ value determined is higher than the value of $2.2x10^{-4}$ $m.s^{-2}$ proposed by Myhr et al. (2001). One

possible explanation of this difference is that the determination of diffusion coefficients is generally carried out using binary alloys. However, interaction of the different alloying elements may result in diffusion rates that deviate significantly from the rates in binary alloys as found by Nicolas and Deschamps (2003) and Kamp et al. (2006) for 7xxx alloys. An interfacial energy value of 0.8 $J.m^{-2}$ may seem too high to be representative of the precipitation of small coherent precipitates (as β″) but is not unrealistic for the precipitation of larger semi-coherent coarsened precipitates. Interfacial energies reported for fully coherent particles in aluminium are generally in the order of 0.2 $J.m^{-2}$ and those reported for incoherent precipitates can reach 1 $J.m^{-2}$. Grong (1997) and Samaras (2006) proposed a value of 0.5 $J.m^{-2}$ for Mg_2Si precipitates. The value used by Myhr et al. (2001) is 0.26 $J.m^{-2}$ but refers to precipitates with a chemical composition assumed to be Mg_5Si_3 and a molar volume of $7.62x10^{-5}$ $m^3.mol^{-1}$. As argued by these authors this choice of a constant interfacial energy can explain the discrepancy between simulation and experiments in the overageing response, since the formation of a fully incoherent phase cannot thus be accounted for in the simulations.

Although the model gives an accurate description of the precipitate radius and the particle number density evolution before the overageing state, Figure 6 shows that predicted room temperature hardness for 1h to 3h of ageing is overestimated. Furthermore, and according to the predicted kinetics, hardness is also overestimated when the alloy is overaged. Further validation of the precipitation or the hardening model is therefore required to better predict the hardness. Nevertheless the hardness is well described for ageing times close to peak hardening, which is already of practical importance since we are concerned here with the simulation of FSW of an Al-Mg-Si alloy in a peak-aged condition.

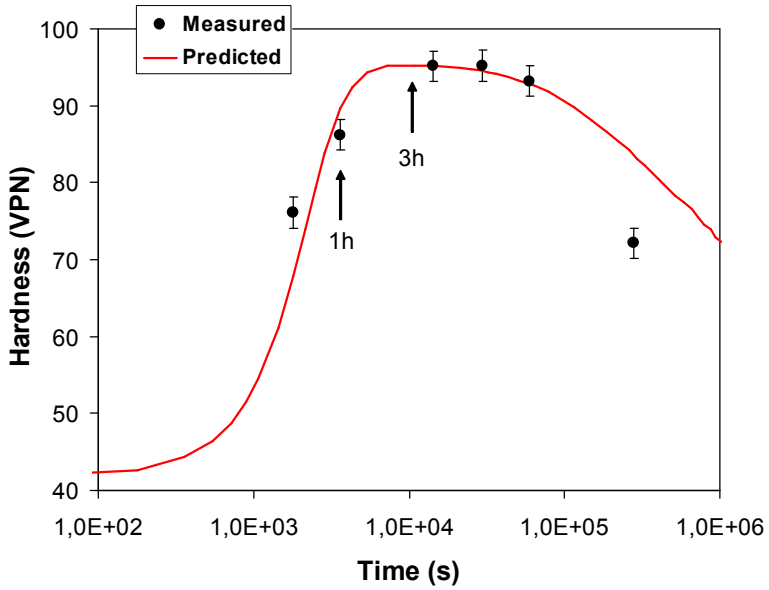

Figure 6. Comparison between predicted and measured room temperature hardness evolution for the experimental Al-Mg-Si alloy during ageing at 185°C. Experimental data from Myhr et al. (2001)

7.2 Application to FSW

As seen in Table 1 the composition of the 6082 alloy used in this work differs slightly from that of the experimental Al-Mg-Si alloy. In particular the magnesium concentration is higher. So according to equation (13), the volume fractions of precipitates at peak ageing will also be higher. With a mean radius still close to the critical radius r_c, higher hardness at peak ageing is thus expected according to equation (26). This is consistent with the measured hardness of the 6082-T651 alloy which is 10 HV more than the hardness of the experimental peak aged Al-Mg-Si alloy. Without further information about the experimental mean radius or the particle number density in the 6082-T651 alloy, this peak hardness value of 105 HV and a corresponding mean radius of about r_c = 5 nm are the two results which have been considered as representative of a correct simulation of the peak-aged T651 condition. The microstructure and strength simulations were achieved with the same input data used for the experimental Al-Mg-Si alloy, except for the value of $k_{\Delta G^*}$ which was taken to be 0.0054. This actually leads to a predicted mean radius of 4.95 nm and a hardness of 106.1 HV after 8h at 175°C (peak-aged condition for 6082 alloy, see Table 2). Using the thermal model described in section 3, the temperature history was predicted at 31 points at mid-thickness of the plate where hardness was measured. At each point, the peak

ageing condition was first simulated, then the welding thermal cycle was applied. Experimental and predicted (with and without NA modelling) hardness transverse variations are shown in Figure 7.

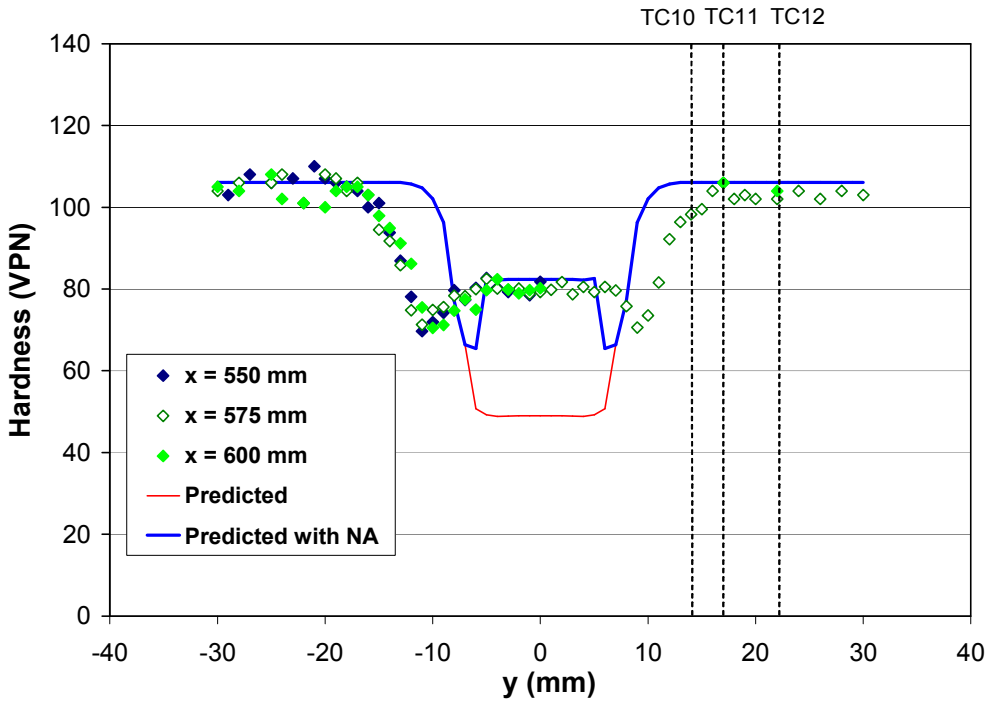

Figure 7. Comparison between predicted (x = 600 mm) and measured hardness variation at mid-thickness for the FS welded 6082-T651 plate. Locations of thermocouples TC10, TC11 and TC12 are shown.

Since $k_{\Delta G^*}$ was optimised to correctly simulate the peak aged condition, it is not surprising that the model accurately predicts the base metal hardness. When NA is taken into account by the strength model, the hardness close to the weld line is also accurately predicted. The model predicts the softening in the HAZ upon approaching the weld line but the predicted width of the HAZ is too narrow. The minimum hardness is only slightly underestimated but the point of minimum hardness is consistently too close to the weld line. A noticeable softening is thus predicted at 11-12mm from the weld line instead of 15-16 mm in the experimental hardness evolution. This is the most significant discrepancy between predicted and experimental hardness. This may be a result of an underestimation of the amount of dissolution caused by a poor optimisation of the microstructure model parameters or because the thermal model may underestimate the temperature near the tool. One can also note that the microstructure model could be improved by taking into account the multicomponent character of the 6xxx aluminium alloys as in Svoboda et al. (2004) or Gallais et al (2008).

In order to check if the sequence of reactions occurring during FSW of the alloy was well captured, the predicted microstructure evolution at 9 mm from the welded line was analysed. Figure 8(a) shows the thermal history, where the peak temperature within the HAZ is seen to reach 350°C. Figure 8(b) shows the mean radius and the corresponding change in the particle number density as a function of time. The mean matrix Mg concentration and the precipitate volume fraction evolution are shown in Figure 8(c).

Starting from the peak aged condition, the fast increase to 350°C implies that both the mean radius and the particle number density drop initially as a result of particle dissolution. There is thus a corresponding drop in the precipitate volume fraction and an abundant solute supply in the matrix from the dissolving smallest precipitates. During subsequent cooling, owing to the high level of solute in the matrix, the rapid growth of the largest particles consumes magnesium. Consequently the mean radius and the precipitate volume fraction increase until the temperature becomes too low. This is in complete accordance with the β″-dissolution and the β′-precipitation phenomena occurring in FSW HAZ (Svennson et al., 2000; M.J. Peel et al., 2006).

Close to the weld line (not shown here) the peak temperature was sufficiently high to achieve a full reversion of the precipitates but, as expected, the fast cooling prevents the re-precipitation process. This region has a high level of solute in the matrix immediately after welding, and is therefore subject to natural ageing within a few

days after FSW. The precipitation of GP zones leads to an increase in hardness measured in subsequent experiments.

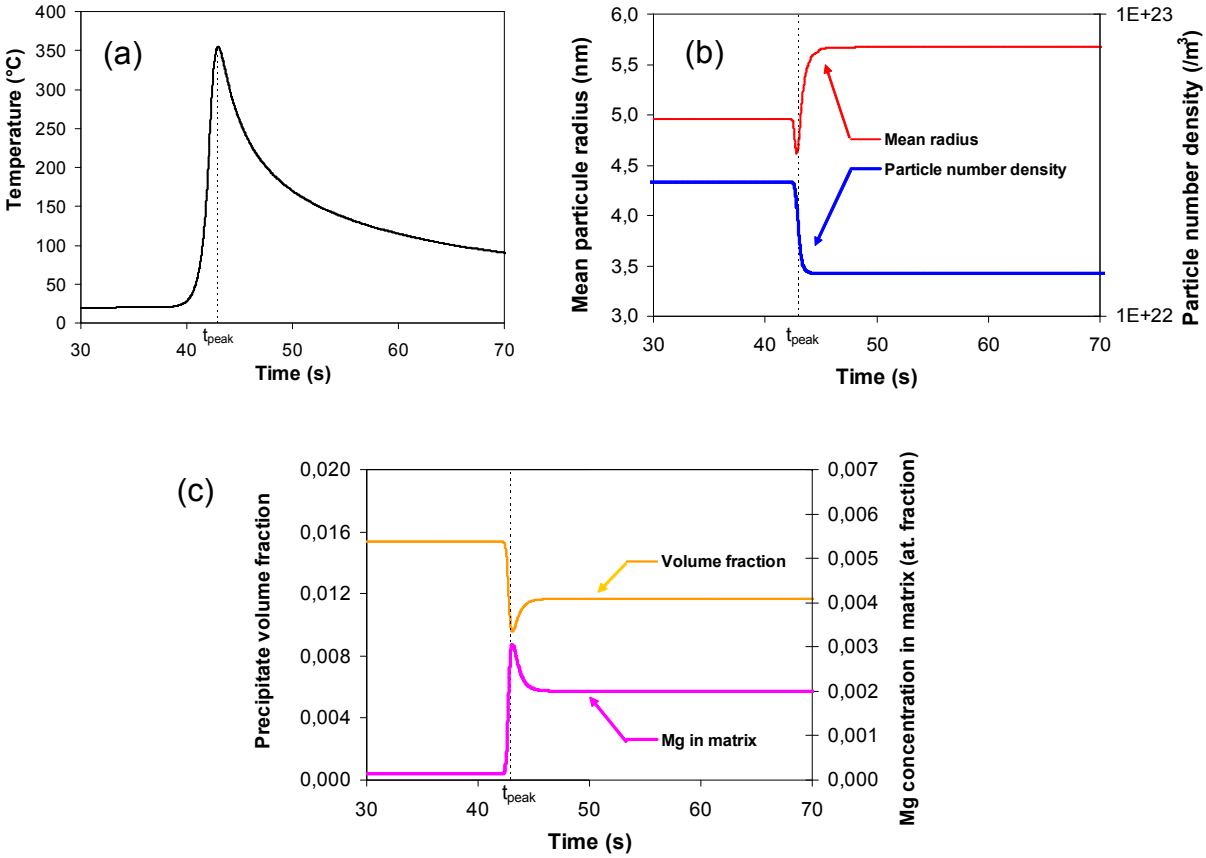

Figure 8. Predicted microstructural evolution during FSW of 6082-T651 plate (x = 600 mm, y = 9 mm, z = 3 mm): (a) thermal history, (b) change in mean particle radius and particle number density with time, (c) change in matrix Mg concentration and precipitate volume fraction with time.

8 Conclusions

This work adresses microstructural evolution modelling during FSW of an Al-Mg-Si alloy. Experimental data have been produced during the welding of 6 mm thick AA 6082 plates. The temperature evolution has been measured at different locations and hardness measurements were performed across the weld and the parent plates. A FE model has been generated for heat transfer analysis of FSW. Microstructural evolution in the alloy has been modelled using a recently developed metallurgical model coupling a Monte Carlo random sampling technique and classical nucleation and growth theory. This model, initially developed for ferritic steels, has been adapted for prediction of precipitation and hardness in 6xxx aluminium alloys. Some of the model parameters were calibrated from microstructure and hardness data available in the open literature. The model has been applied using temperatures cycles obtained from the FE analysis, and predicted hardness has been compared with the measured data.. The overall hardness profile is well predicted if natural ageing is taken into account, but the extent of the HAZ is under-estimated. Nevertheless the sequence of reactions occurring during FSW of the alloy is well captured by the model. Observed discrepancies could have been caused by an underestimation of the temperature near the tool by the thermal model. However improvement of the precipitation model is also suggested through a better optimisation of the model parameters and the consideration of the multicomponent character of the alloy.

Aknowledgments

D. Carron thanks Loughborough University, the Université de Bretagne-Sud (France) and the Ministère de l'Enseignement Supérieur et de La Recherche (France) for making possible a six month visiting period at Loughborough University.

References

Alcan: *Aluminium and the sea*, Alcan Marine, France (2004).

Chakrabartia, D.J.; Laughlin, D. E.: Phase relations and precipitation in Al-Mg-Si alloys with Cu additions. *Prog. in Mat. Sci.*, 49, (2004), 389-410.

Deschamps, A.; Brechet, Y.: Influence of predeformation on ageing in an Al-Zn-Mg alloy - part II : Modeling of microstructure evolution and mechanical properties. *Acta Mater*., 47, (1999), 293-305.

Esmaeili, S., Lloyd, D.J.; Poole W.J.: Modeling of precipitation hardening for the naturally aged Al-Mg-Si-Cu alloy AA6111. *Acta Mater.*, 51, (2003), 3467–3481.

Faulkner, R.G.: Combined grain boundary equilibrium and non-equilibrium segregation in ferritic/martensitic steels. *Acta met*., 35, (1987), 2905-2914.

Friedel, J.: *Dislocations.* Pergamon Press, Oxford, UK (1964).

Gallais, C.; Denquin, A.; Bréchet, Y.; Lapasset, G.: Precipitation microstructures in an AA6056 aluminium alloy after friction stir welding : Characterisation and modelling. *Mat. Sci. and Engng. A*, 496, (2008), 77-89.

Grong, O.: *Metallurgical Modelling of Welding 2nd ed.* The Institute of Materials, London, UK (1997).

Hatch, J.E.: *Aluminium-properties and physical metallurgy.* Metals Park: OH, American Society for Metals, USA (1984).

Kamp, N.; Sullivan, A.; Tomasi, R.; Robson, J.D.: Modelling of heterogeneous precipitate distribution evolution during friction stir welding process. *Acta Mater*., 54, (2006), 2003-2014.

Kamp, N.; Sullivan, A.; Robson, J.D.: Modelling of friction stir welding of 7xxx aluminium alloys, *Mat. Sci. and Engng. A*, 466, (2007), 246-255.

Kampmann, R.; Wagner, R.: *Materials Science and Technology vol.5*. VCH-Weinheim, Germany (1991).

Myhr, O.R.; Grong, O.; Andersen S.J.: Modelling of the age hardening behaviour of Al-Mg-Si alloys. *Acta Mater.*, 49, (2001), 65-75.

Mishra, R.S.; Ma, Z.Y.: Friction stir welding and processing. *Mat. Sci. Engng. Reports*, 50, (2005), 1-78.

Nicolas, M.; Deschamps, A.: Characterisation and modelling of precipitate evolution in an Al-Zn-Mg alloy during non-isothermal heat treatments. *Acta Mater*., 51, (2003), 6077-6094.

Peel, M.J.; Steuwer, A.; Withers, P.J.: Dissimilar Friction Stir Welds in AA5083-AA6082. Part II: Process Parameter Effects on Microstructure. *Met. and Mat. Trans. A*, 37, (2006), 2195-2206.

Perez M.: Gibbs–Thomson effects in phase transformations. *Scripta mater.*, 52, (2005), 709-712.

Perez, M.; Dumont, M.; Acevedo-Reyes, D.: Implementation of classical nucleation and growth theories for precipitation. *Acta Mater.,* 56, (2008), 2119-2132.

Ravi, C.; Wolverton, C.: First-principles study of crystal structure and stability of Al-Mg-Si-(Cu) precipitates. *Acta Mater.*, 52, (2004), 4213-4227.

Robson, J.D.; Sullivan, A.; Shercliff, H.R.; McShane, G.: Microstructural evolution during friction stir welding of AA7449. In : *Proceedings of the 5th International Symposium on Friction Stir Welding.* September, Metz, France, (2004).

Russell, M.J.; Shercliff, H.R.: Analytical modelling of microstructure development in friction stir welding. In: *Proceedings of the 1st International Symposium on Friction Stir Welding*. June, Thousand Oaks, CA, USA, (1999).

Samaras, S.N.: Modelling of microstructure evolution during precipitation processes: a population balance approach of the KWN model. *Model. and Sim. in Mat. Sci. Engng.,* 14, (2006), 1271-1292.

Simar A., Lecomte-Beckers, J; Pardoen, T.; de Meester, B.: Effect of boundary conditions and heat source distribution on temperature distribution in friction stir welding. *Sci. Tech. Weld. Join.,* 11, (2006), 170-177.

Simar, A.; Brechet, Y.; de Meester, B.; Denquin, A.; Pardoen, T.: Sequential modelling of local precipitation, strength and strain hardening in friction stir welds of an aluminium alloy 6005A-T6, *Acta Mater.*, 55, (2007), 6133-6143.

Smith, S.D.: Validation of analytical and computational model of friction stir welding. *TWI member report N° MR816/200*, TWI, Cambridge, UK (2004).

Svoboda, J.; Fischer, F.D.; Fratzl, P.; Kozeschnik E.: Modelling of kinetics in multi-component multi-phase systems with spherical precipitates. *Mat. Sci. and Engng. A*, 385, (2004), 166-174.

Svennson, L.E.; Karlsson, L.; Larsson, H.; Karlsson, B.; Fazzini, M.; Karlsson, J.: Microstructure and mechanical properties of friction stir welded aluminium alloys with special reference to AA 5083 and AA 6082. *Sci. Tech. Weld. Join.*, 5, (2000), 285-296.

Thomas, W.M.; Nicholas, E.D.; Needham, J.C.; Murch, M.G.; Templesmith, P.; Dawes, C.J.: Friction Stir Butt Welding, *International Patent No. PCT/GB92/02203* (1991).

Yin, Y.F; Faulkner, R.G.: Simulation of precipitation in ferritic steels. *Mater. Sci. Technol.*, 19, (2003), 91-98.

Yin, Y.F; Faulkner, R.G.: Creep damage and grain boundary precipitation in power plant metals. *Mater. Sci. Technol.*, 21, (2005), 1239-1246.

Yin, Y.F; Faulkner, R.G.: Continuum damage mechanics based on simulation of microstructural evolution kinetics. *Mater. Sci. Technol*., 22, (2006), 929-936.

Yin, Y.F; Faulkner, R.G.; Lu, Z.: Irradiation-induced precipitation modelling of ferritic steels. *J. Nucl. Mat.*, 389, (2009), 225–232.

Addresses: Dr. Denis Carron, LIMATB, Université de Bretagne Sud, Rue St Maudé, F-56321 Lorient, France
Dr. Philippe Bastid, NMO Section, TWI Ltd, Granta Park, Great Abington, Cambridge CB1 6AL, UK
Dr. You Fa Yin and Prof. Roy G. Faulkner, Department of Materials, Loughborough University, Ashby Road, Leicestershire LE11 3TU, UK
email: denis.carron@univ-ubs.fr; philippe.bastid@twi.co.uk; y.yin@lboro.ac.uk; r.faulkner@lboro.ac.uk.